Biosensors and Bioelectronics 144 (2019) 111671

Contents lists available at ScienceDirect

Biosensors and Bioelectronics

journal homepage: www.elsevier.com/locate/bios

Modulating near-infrared persistent luminescence of core-shell nanoplatform for imaging of glutathione in tumor mouse model

Yang Feng, Lichun Zhang, Rui Liu, Yi Lv*

Key Laboratory of Green Chemistry & Technology, Ministry of Education, College of Chemistry, Sichuan University, Chengdu, Sichuan, 610064, China

ARTICLE INFO

Keywords:
Near-infrared persistent luminescence
Bioprobe
Core-shell structure
Glutathione imaging

ABSTRACT

Developing near-infrared (NIR) persistent luminescence (PersL) bioprobes has attracted increasing attention due to their ultra-low autofluorescence and deep tissue penetration. Accurate imaging of glutathione (GSH) in vivo is of great significance to provide a real-time visualization of pathologies. Herein, manipulating metal ions as the switch of NIR afterglow was demonstrated to construct NIR PersL nanoprobes for the first time, which was highly efficient and much simpler than the luminescence resonance energy transfer (LRET) principle. As a proof-of-concept application, an activatable NIR PersL nanoprobe (**Probe-1**) built on core-shell structure was rationally fabricated for detection of GSH via employing Cu^{2+} as the quencher. In light of unique NIR PersL feature and flexible functionality, **Probe-1** exhibited greatly enhanced analytical performances for GSH detection, and particularly imaging of tumor in living mouse. This approach without limits of spectral overlap from the LRET principle provided a new way to develop NIR PersL bioprobes for autofluorescence-free detection.

1. Introduction

Optical imaging has drawn more and more attention in recent years due to its merits of high imaging sensitivity, portability, low cost and feasibility for clinical translation (Zhu et al., 2018; Wang et al., 2018a,b; Yuan et al., 2019; Liu et al., 2016). Notably, Persistent luminescence nanoparticles (PLNPs), a kind of fascinating materials emitting persistent luminescence (PersL) after ceasing excitation, have emerged as a promising alternative to traditional tracer molecules (le Masne de Chermont et al., 2007). Such a unique optical feature permits bio-applications ex situ excitation avoiding the interferences of autofluorescence from tissue and scattering light from excitation source (Abdukayum et al., 2013). Particularly, Yan' group firstly reported a PersL nanoprobe with green afterglow for the detection of alpha-fetoprotein in vitro via a luminescence resonance energy transfer (LRET) process, which paves a new pathway for autofluorescence-free bioassays (Wu et al., 2011). Furthermore, other LRET-based PersL nanoprobes with green afterglow have been enriched for the detection of various targets, employing organic dyes (Wang et al., 2017a,b; Feng et al., 2019) or inorganic nanosized materials (Li et al., 2014a,b; Wu et al., 2015; Yuan et al., 2019; Chen et al., 2016) as energy acceptors to regulate the read-out PersL signal. It is clear from the literatures that PersL bioprobe is of ultralow-background and lead to improvement of sensing sensitivity (Sun et al., 2018).

To obtain deeper tissue penetration, near-infrared (NIR, within the tissue transparency window) PLNPs represented by Cr^{3+}-doped gallates have been introduced by Scherman' group (Maldiney et al., 2014). More importantly, $ZnGa_2O_4:Cr^{3+}$ (ZGO) has been found to be re-activated by using tissue-penetrable NIR light, which makes the bio-applications no longer limited by the lifetime of PLNPs (Li et al., 2015). In view of deep-tissue penetration and ultra-low autofluorescence, NIR PersL nanoprobes have shown great potential for bio-sensing applications (Yu et al., 2018). Although the LRET strategy is the most suitable principle to endow the switch signal of the energy donor (PLNPs), the rigorous confines of spectral overlap between the donor-acceptor pair result in limited flexibility in the design of nanoprobe (Li et al., 2016). Thus, fabricating LRET-based NIR PersL nanoprobe has been hampered due to lack of NIR acceptors (Su et al., 2017).

To our best knowledge, heavy metal ions employed as significant quenchers of fluorophores and phosphors have attracted increasing attention (Tang et al., 2013; Liang et al., 2016). However, no follow-up research was seen to pave way for NIR PersL. Herein, we discovered that heavy metal ions especially Cu^{2+} could induce efficient quenching of NIR PersL to degrees of > 95%. On this basis, we proposed a new approach by manipulating heavy metal ions as the switch of optical signal to develop NIR PersL nanoprobes. This method, free from matching spectra, could be uncomplicated and more straightforward.

Attractively, glutathione (GSH) served as the most plentiful

* Corresponding author.
E-mail address: lvy@scu.edu.cn (Y. Lv).

https://doi.org/10.1016/j.bios.2019.111671
Received 24 May 2019; Received in revised form 27 August 2019; Accepted 31 August 2019
Available online 03 September 2019
0956-5663/

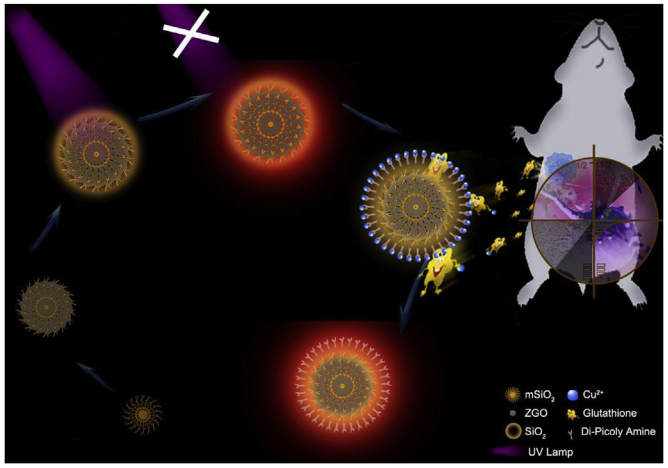

Scheme 1. Schematic illustration of the design principle, synthetic route and applications for GSH imaging of **Probe-1**.

intracellular thiol plays key roles in pathological conditions (Li et al., 2018; Fu et al., 2019; Liu et al., 2017). More significantly, GSH has been reported to have much higher concentration in cancer cells than that in normal cells, making it one of the most important signal molecules to diagnose cancer. Inspired by the unique interaction between Cu^{2+} and GSH, a proof-of-concept NIR PersL nanoprobe (CSZGO-DPA-Cu^{2+}; designated as **Probe-1**) was rationally constructed for detection of GSH employing Cu^{2+} as the quencher (Scheme 1). Note that, both flexible functionality and uniform morphology of **Probe-1** were foremost ensured, which were of great significance for reliable and distinguished sensing performance. The core-shell architecture of ZGO (CSZGO) was fabricated to integrate functional modalities (Zou et al., 2017). Thereafter, the quencher was anchored to ligand DPA (Di-(2-Picoly) Amine) molecules on the surface of CSZGO through weakly-bond. The NIR PersL intensity was recovered upon the removal of Cu^{2+} on the surface for the first time, which enabled NIR PersL detection of GSH. In light of autofluorescence-free background and deep-tissue penetration, **Probe-1** demonstrated excellent analytical performances for GSH detection and particularly imaging of tumor in living mice.

2. Experimental section

Details on materials, apparatus and experimental procedures performed in this work can be found in the Supplementary Information.

3. Results and discussion

3.1. Synthesis and characterization of CSZGO

To obtain uniform and mono-dispersed NIR PLNPs, the mesoporous silica ($mSiO_2$) as morphology-controlling templates was firstly synthesized. As shown in the transmission electron microscopy (TEM) and scanning electron microscopy (SEM) images (Fig. 1A, Fig. 1D and Fig. S1A, ESI†), $mSiO_2$ showed a regular mesoporous morphology and a narrow size distribution (~160 nm). Moreover, the regular mesostructured of $mSiO_2$ was strongly evidenced via the corresponding nitrogen adsorption-desorption isotherm (Fig. S2, ESI†). The surface area and average pore size of the $mSiO_2$ was measured to be approximately 511.69 $m^2 g^{-1}$ and 6.4 nm, respectively by brunauer – Emmett – Teller (BET) and barrett–Joyner–Halenda (BJH) analysis (Fig. S2, ESI†).

Leveraging on the regular center-radial mesostructured of $mSiO_2$, the ZGO@$mSiO_2$ was further prepared by ionic impregnation and post annealing. Satisfyingly, the uniform morphology and mono-dispersity maintained well after calcination. Meantime, many distributed black spots isolated in pore channels were observed (Fig. 1B and E and Fig. S1B, ESI†). And the BET surface area showed a remarkably decrease from 511.69 $m^2 g^{-1}$ to ~164.36 $m^2 g^{-1}$, further supporting the formation of ZGO@$mSiO_2$ (Fig. S2, ESI†). Moreover, the actual composition of ZGO@$mSiO_2$ was displayed by elemental mapping analysis that the Zn and Ga elements were evenly distributed throughout the $mSiO_2$ matrix (Fig. 2A). The HRTEM image taken at the edge of a selected black spot showed that a 0.147 nm uniform lattice fringe of d-spacing for (440) lattice plane of the PLNPs was consistent with the cubic spinel structure of ZGO (Fig. 2B) (Wang et al., 2018a,b). Besides, a multicrystalline feature of ZGO@$mSiO_2$ was presented by x-ray diffraction (XRD) patterns (Fig. S3, ESI†) and SAED pattern (Fig. 2B, Insert). Above all, these results explained the existence of ZGO tiny particles as isolated inside the pores of the $mSiO_2$.

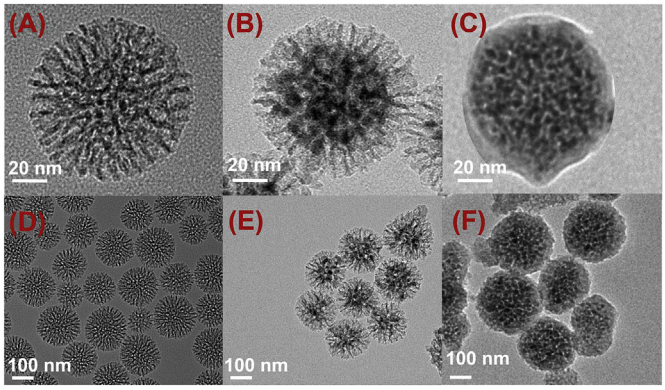

Fig. 1. TEM images of $mSiO_2$ (A, D); ZGO@$mSiO_2$ (B, E); CSZGO (C, F).

To improve water dispersion and increase active sites, the CSZGO was subsequently designed through SiO_2 shell encapsulated, which possessed a uniform core-shell structure with a thickness of shell about 2.8 nm (Fig. 1C and F and Fig. S1C, ESI†). Significantly, the zeta potential changed from −9.4 mV to −38.1 mV, indicating more negative active sites increased (Fig. 3A). It was worthy noticing that the size distribution in PBS of CSZGO showed better stability (Fig. S4, ESI†). Collectively, the CSZGO with a highly regular spherical morphology and flexible functionality were successfully obtained.

3.2. Luminescence performance of CSZGO

Considering the significance of excellent NIR afterglow for further bio-applications, some key luminescence performance of CSZGO were next assessed. As shown in Fig. 2C, the photoluminescence spectra of CSZGO showed an efficient NIR emission located at 712 nm attributed to the $^2E \rightarrow {}^4A_2$ transition of Cr^{3+} under the 257 nm excitation (Wang et al., 2018a,b). As shown in Fig. 2D, the PersL spectra of CSZGO revealed a clear and sharp emission band featured with 712 nm within the NIR region. The satisfied and stable NIR PersL signal was demonstrated by calculated RSD results, which made the CSZGO suitable for bioanalysis (Fig. 2D). For a more intuitive experience, the NIR PersL images of CSZGO were recorded at different time ex situ excitation and even reactivated by a NIR LED lamp (Fig. S5, ESI†). Overall, a highly effective NIR PersL nanoplatform capable of uniform morphology, flexible surface engineering, ultra-low autofluorescence and deep-tissue penetration was constructed, which held great potential for in vivo imaging.

3.3. Fabrication of an activable NIR PersL bioprobe for GSH detection

During the course of our exploration on NIR PersL, we discovered the NIR afterglow signal could be effectively quenched upon addition of the Cu^{2+} (Fig. S6, ESI†). Inspired by the modulation of the afterglow properties of CSZGO by Cu^{2+} and a pulse voltammetry method for thiols detection (Huang et al., 2016; Liu et al., 2015), we employed DPA molecules capable of recognizing and anchoring Cu^{2+} to fabricate GSH-

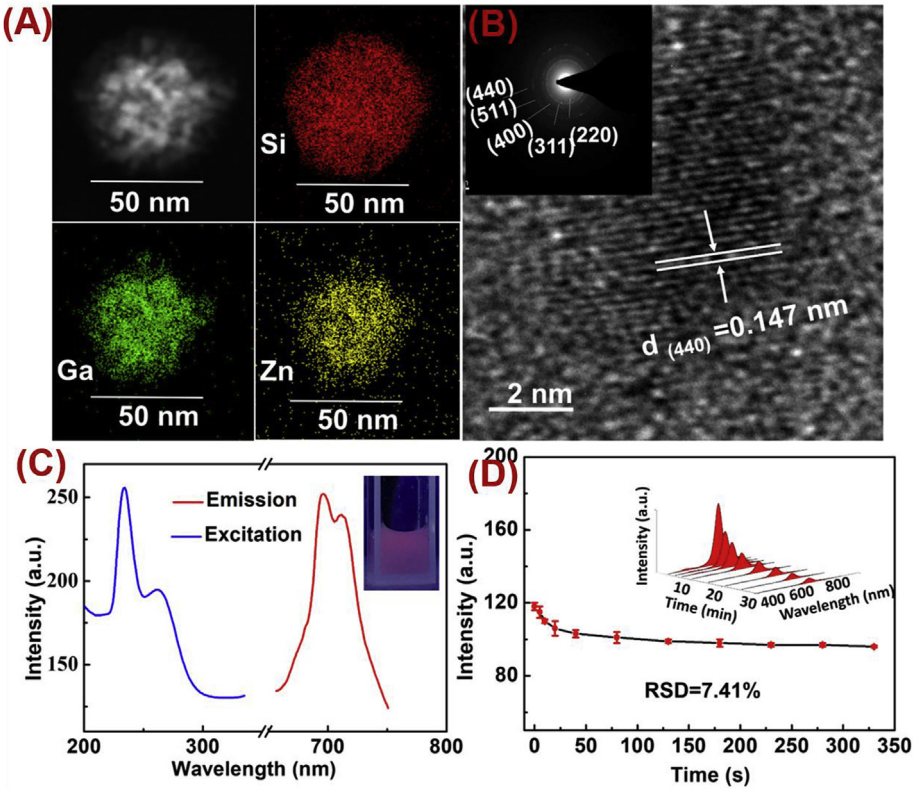

Fig. 2. (A) Elemental mapping images of ZGO@mSiO$_2$; (B) High resolution TEM images of the ZGO@mSiO$_2$. Insert: SAED pattern of the ZGO@mSiO$_2$; (C) Excitation and emission spectra of CSZGO; (D) The band and intensity of NIR PersL emission spectra of the CSZGO.

responsive **Probe-1**. The PAA polymer was fist modified on surface of CSZGO to covalently linked on the surface of CSZGO, which confirmed by a new absorption band at 1712 cm^{-1} for stretching vibration of COO$^-$ (Fig. 3B). And DPA molecules were further conjugated via the formation of amide bond between the amino group of DPA and the carboxyl group of CSZGO-PAA. It could be presented by FT-IR analysis that an appearance of the characteristic band for –CONH- at ~1643 nm^{-1} appeared (Fig. 3B). Additionally, the zeta potential caused a significantly positive shift from −49.3 mV to −26.1 mV after DPA functionalized (Fig. 3A). Furthermore, it could also be presented a new absorption band appeared at 263 nm of DPA molecules (Fig. 3C). Interestingly, anchoring Cu^{2+}, at relatively lower concentration

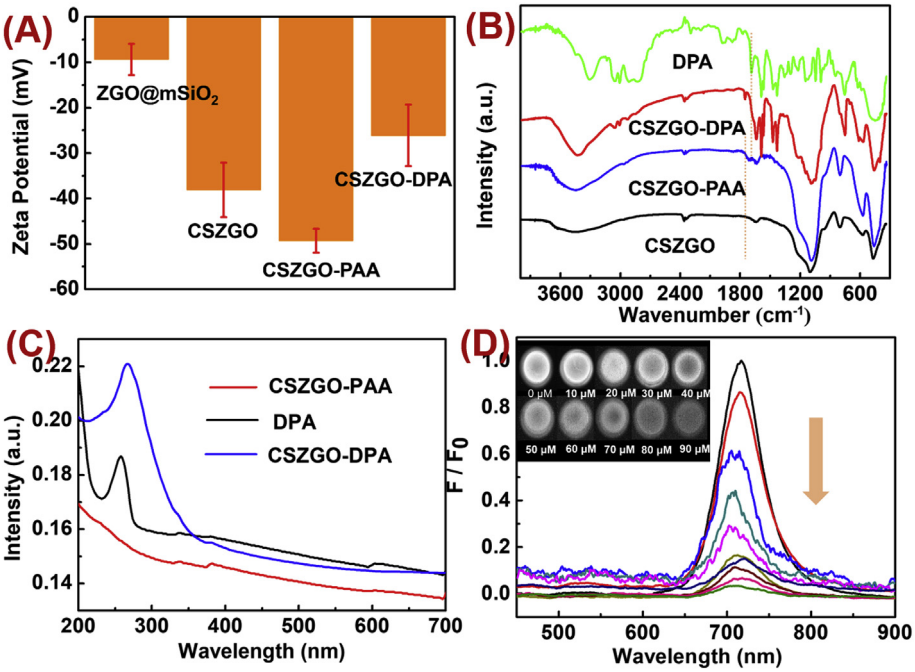

Fig. 3. (A) Zeta potential; (B) FT-IR spectra; (C) UV–vis spectra; (D) Changes in NIR PersL spectra of 1 mg/mL solution of CSZGO-DPA upon gradual conjugation of Cu^{2+}. Insert: the NIR afterglow images under different concentrations of Cu^{2+} were photographed.

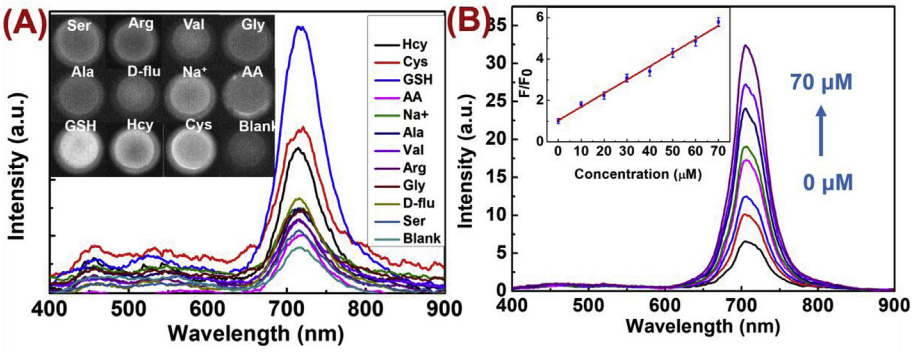

Fig. 4. (A) NIR afterglow intensity of **Probe-1** (800 μg/mL) upon addition of various completing species. Insert: the images of NIR PersL; (B) NIR PersL response of **Probe-1** nanoprobe (800 μg/mL) as a function of GSH concentration in an aqueous solution. Insert: plot of luminescence intensity at 712 nm against the GSH concentration.

(90 μM), onto the surface of CSZGO-DPA induced a significant quenching of NIR PersL to degrees of > 95% (Fig. 3D). The insert image of Fig. 3D was further displayed the instinctive changes of quenched afterglow. Note that, such a noble quenching efficiency become a key point to keep minimal background signal and even improve the detection sensitivity to a great extent. It should also be mentioned that simply physically mixing the CSZGO with Cu^{2+} did not show obvious quenching under the same concentration. The existence of Cu^{2+} was further confirmed by EDS data (Fig. S7, ESI†). Moreover, the lifetimes decreased from 0.015 m s to 0.011 m s, indicating the existence of non-static quenching (Fig. S8, ESI†). Thereafter, the activatable **Probe-1** was successfully fabricated.

3.4. GSH sensing performance of *Probe-1*

To examine the selectivity of **Probe-1** for the detection of GSH, a range of potentially competing species such as Na^+ (0.18 mM), AA, L-Cys, L-Arg, Ser, Val, Ala, D-flu, Gly and Hcy (100 μM) was explored. As shown in Fig. 4A, a remarkable enhancement of the NIR emission intensity appeared while GSH (100 μM) was introduced, demonstrating that **Probe-1** could detect GSH over other anions with high sensitivity and selectivity. More attractively, it was also visual for imaging of GSH in vitro (Fig. 4A, Insert). This observation was explained that the particularly stable species of Cu^{2+} and GSH could remove Cu^{2+} from other weakly-bond surfaces of **Probe-1**. The NIR afterglow was thereafter recovered due to the prolonged distance (quencher-donor). Moreover, the kinetic curve of the **Probe-1** upon the addition of GSH was explored by time-dependent fluorescence spectroscopy. The complete enhancement of the NIR PersL intensity occurred within 8 min after introduced GSH to **Probe-1** (Fig. S9, ESI†). With this in mind, we next sought to the sensitivity of **Probe-1** after titration of various amounts of GSH. In particular, the NIR emission showed linearity to the amounts of GSH ranging from 0 to 70 μM, with correlation coefficient of 0.998 (Fig. 4B). Due to ex situ excitation, this approach had a low detection limit of (LOD) 0.35 μM. Overall, **Probe-1** demonstrated excellent analytical performances in vitro.

3.5. GSH imaging in living cells and in vivo

Prior to applying **Probe-1** for biological imaging, the cytotoxicity of **Probe-1** with 231 cells and HL-7702 cells was investigated by CCK-8 assay. The cellular viability of **Probe-1** was estimated to be > 85% after incubation with 1.0 mg/mL of the **Probe-1** for 48 h, which illustrated **Probe-1** was safe for living cells (Fig. S10, ESI†). In addition, the monitoring of the **Probe-1** NIR PersL response showed that **Probe-1** was stable in the pH range from 6 to 8, which was also suitable for the further detection of GSH under the physiological conditions (Fig. S11, ESI†). To confirm the capability of **Probe-1** for monitoring intracellular GSH levels in cancer cells, the practical utility of **Probe-1** for GSH detection in living 231 tumor cells was then investigated by Caliper IVIS Lumina III imaging system. Obvious NIR PersL signal in the tumor cells was observed (Fig. S12, ESI†). In contrast with this result, weaker NIR PersL was found in 231 cells pre-treated with NMM (a well-known thiols trapping reagent). Meanwhile, stronger NIR PersL was shown in 231 cells pre-treated with GSH. Furthermore, the capability of **Probe 1** to sense differential levels of GSH produced by healthy and cancer cells in vitro was carried out. As shown in Fig. S13 (ESI), **Probe-1** cultured in cancer cells exhibited a clear enhancement of NIR PersL compared with normal cells over time, demonstrating excellent sensitivity for monitoring GSH in living cells. These results demonstrated that **Probe-1** possessed the ability of imaging cancer cells and could sensitively monitor abnormal levels of GSH in living cells.

To further evaluate the capability of **Probe-1** for visualization of GSH in vivo, 231 tumor-bearing mice were respectively injected with **Probe-1** in tumoral and non-tumoral areas, and then in vivo NIR PersL images were monitored by an IVIS imaging system over time. Interestingly, within 10 min post-injection of the **probe-1**, stronger NIR PersL signal in the tumor site appeared (Fig. 5). Moreover, this specific signal in the tumors enhanced remarkably compared with healthy tissues over time and reached a plateau within 30 min after **Probe-1** injection. In addition, the mice were pre-treated with NMM (NMM, a GSH scavenger) in tumor region and then respectively injected with Probe-1 in tumoral and non-tumoral areas. As shown in Fig. S14 (ESI), a dramatically lower intensity of NIR PersL was observed within 40 min, indicating that GSH is responsible of the afterglow levels detected at the tumor site. Undoubtedly, **Probe-1** was successfully applied for sensitive detection endogenous GSH in vivo. Above all, these results indicated that **Probe-1** has excellent bio-sensing performances and outstanding tissue penetrating for GSH detection in vivo, which showed great potential for a real-time visualization of physiological conditions.

To evaluate the toxicity of **Probe-1** in vivo, the weight of each mice was fist carried out. As shown in Fig. S15 (ESI), the negligibly weight changes of the mice were observed, indicating low systemic toxicity of the **Probe-1**. Moreover, histological analysis of major organs from mice was performed after 15 days. In comparison to that in the control group, no noticeable damage sign of the organs such as liver, spleen, heart, lung, and kidney was found (Fig. S16, ESI). The cumulative waste of the **Probe-1** was further studied. The result showed that 72.3% of the nanoparticles were excreted of mice in 14 days after intramuscular injection (Fig. S17, ESI). In addition, **Probe-1** mainly accumulated in the liver and spleen in the first 8 h (Fig. S18, ESI). All these results proved that **Probe-1** was a biocompatible and efficient technique for in vivo imaging.

4. Conclusions

In summary, employing heavy metal ions as the signal regulator was developed to fabricate NIR PersL nanoprobes for the first time, which featured simplicity, high efficiency and extendibility. As a proof-of-concept application, the efficient NIR PersL bioprobe built on core-shell structure was rationally designed, which demonstrated lower auto-fluorescence and deeper penetration for NIR afterglow imaging of GSH

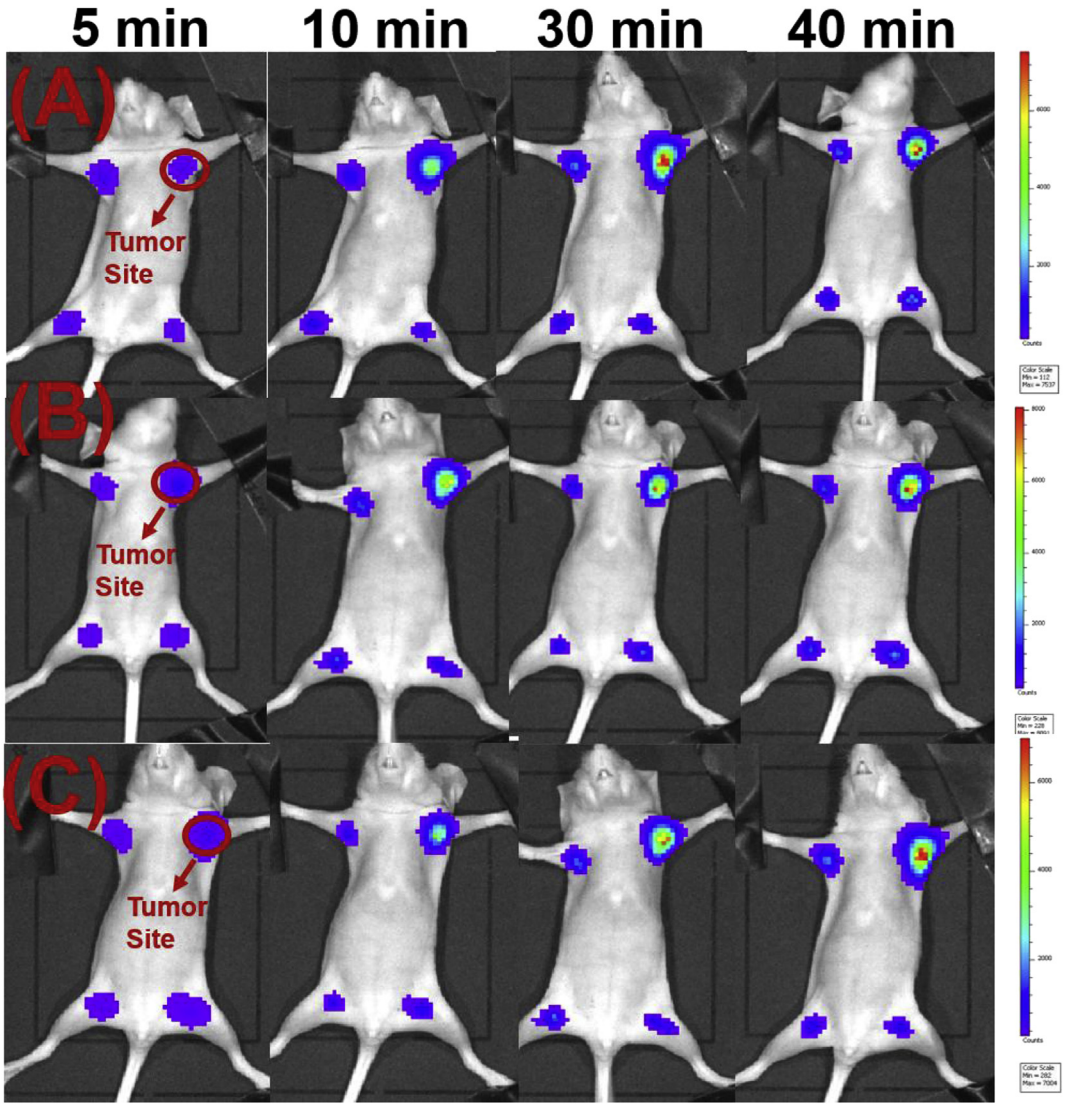

Fig. 5. The NIR PersL images in tumoral and non-tumoral areas of the same mice at indicated time points after injection of **Probe-1** (A); and repeated for two times under the same conditions (B–C).

in vitro and in vivo. This approach opened a new way to develop NIR PersL bioprobes with no need of spectral overlap or introduction of limited energy acceptors.

CRediT authorship contribution statement

Yang Feng: Conceptualization, Methodology, Software, Investigation, Formal analysis, Writing - original draft. **Lichun Zhang:** Writing - review & editing, Data curation, Validation. **Rui Liu:** Writing - review & editing, Resources. **Yi Lv:** Supervision, Project administration.

Declaration of competing interest

The authors declare that they have no known competing financial interests or personal relationships that could have appeared to influence the work reported in this paper.

Acknowledgements

This work was supported by the National Natural Science Foundation of China (Nos. 21675113 & 21575093) and the Fundamental Research Funds for the Central Universities (Grant 2018SCUH0078). We thank Xu Peng in Experimental Animal Center of Sichuan University, Prof. Shanling Wang and Dr. Shuguang Yan in Analytical & Testing Center at Sichuan University for their generous technique supporting.

Appendix A. Supplementary data

Supplementary data to this article can be found online at https://doi.org/10.1016/j.bios.2019.111671.

References

Abdukayum, A., Chen, J.T., Zhao, Q., Yan, X.P., 2013. J. Am. Chem. Soc. 135 (38), 14125–14133.
Chen, L.J., Sun, S.K., Wang, Y., Yang, C.X., Wu, S.Q., Yan, X.P., 2016. ACS Appl. Mater. Interfaces 8 (48), 32667–32674.
Feng, Y., Deng, D.Y., Zhang, L.C., Liu, R., Lv, Y., 2019. Sens. Actuators B Chem. 279, 189–196.
Fu, X.-L., Hou, F., Liu, F.-R., Ren, S.-W., Cao, J.-T., Liu, Y.-M., 2019. Biosens. Bioelectron. 129, 72–78.
Huang, Y., Zhou, J., Feng, H., Zheng, J., Ma, H.-M., Liu, W., Tang, C., Ao, H., Zhao, M., Qian, Z., 2016. Biosens. Bioelectron. 86, 748–755.
le Masne de Chermont, Q., Chaneac, C., Seguin, J., Pelle, F., Maitrejean, S., Jolivet, J.P., Gourier, D., Bessodes, M., Scherman, D., 2007. Proc. Natl. Acad. Sci. U.S.A. 104 (22), 9266–9271.
Li, N., Li, Y.H., Han, Y.Y., Pan, W., Zhang, T.G., Tang, B., 2014a. Anal. Chem. 86 (8),

3924–3930.
Li, N., Diao, W., Han, Y., Pan, W., Zhang, T., Tang, B., 2014b. Chem. Eur J. 20 (50), 16488–16491.
Li, Z.J., Zhang, Y.W., Wu, X., Huang, L., Li, D.S., Fan, W., Han, G., 2015. J. Am. Chem. Soc. 137 (16), 5304–5307.
Li, Y., Gecevicius, M., Qiu, J.R., 2016. Chem. Soc. Rev. 45 (8), 2090–2136.
Li, Z., Zhang, J., Li, Y., Zhao, S., Zhang, P., Zhang, Y., Bi, J., Liu, G., Yue, Z., 2018. Biosens. Bioelectron. 99, 251–258.
Liang, T., Li, Z., Song, D., Shen, L., Zhuang, Q., Liu, Z., 2016. Anal. Chem. 88 (20), 9989–9995.
Liu, Z., He, W., Pei, M., Zhang, G., 2015. Chem. Commun. 51 (75), 14227–14230.
Liu, Y., Gong, X.J., Cheng, Z., Shuang, S.M., Choi, M.M.F., Li, C.Z., Dong, C., 2016. RSC Adv. 6 (91), 88042–88049.
Liu, J., Meng, L., Fei, Z., Dyson, P.J., Jing, X., Liu, X., 2017. Biosens. Bioelectron. 90, 69–74.
Maldiney, T., Bessiere, A., Seguin, J., Teston, E., Sharma, S.K., Viana, B., Bos, A.J.J., Dorenbos, P., Bessodes, M., Gourier, D., Scherman, D., Richard, C., 2014. Nat. Mater. 13 (4), 418–426.
Su, Q., Feng, W., Yang, D., Li, F., 2017. Accounts Chem. Res. 50 (1), 32–40.
Sun, S.-K., Wang, H.-F., Yan, X.-P., 2018. Accounts Chem. Res. 51 (5), 1131–1143.
Tang, Y.R., Song, H.J., Su, Y.Y., Lv, Y., 2013. Anal. Chem. 85 (24), 11876–11884.
Wang, P., Wang, Q., Huang, J., Li, N., Gu, Y., 2017a. Biosens. Bioelectron. 92, 583–588.
Wang, J., Ma, Q., Hu, X.X., Liu, H., Zheng, W., Chen, X., Yuan, Q., Tan, W.H., 2017b. ACS Nano 11 (8), 8185–8191.
Wang, J., Li, J., Yu, J., Zhang, H., Zhang, B., 2018a. ACS Nano 12 (5), 4246–4285.
Wang, H.-F., Chen, X., Feng, F., Ji, X., Zhang, Y., 2018b. Chem. Sci. 9 (48), 8923–8929.
Wu, B.Y., Yan, X.P., 2015. Chem. Commun. 51 (18), 3903–3906.
Wu, B.Y., Wang, H.F., Chen, J.T., Yan, X.P., 2011. J. Am. Chem. Soc. 133 (4), 686–688.
Yu, Z.Z., Liu, B., Pan, W., Zhang, T.T., Tong, L.L., Li, N., Tang, B., 2018. Chem. Commun. 54 (28), 3504–3507.
Yuan, R.Q., Ma, Y.H., Du, J.Y., Meng, F.X., Guo, J.J., Hong, M., Yue, Q.L., Li, X., Li, C.Z., 2019. Anal. Methods 11 (11), 1522–1529.
Zhu, B., Wu, L., Zhang, M., Wang, Y., Liu, C., Wang, Z., Duan, Q., Jia, P., 2018. Biosens. Bioelectron. 107, 218–223.
Zou, R., Gong, S., Shi, J., Jiao, J., Wong, K.-L., Zhang, H., Wang, J., Su, Q., 2017. Chem. Mater. 29 (9), 3938–3946.